

N-body self-consistent stars-halo modeling of the Fornax dwarf galaxy

GALINA SHCHELKANOVA,¹ KOHEI HAYASHI,^{2,3} AND SERGEI BLINNIKOV^{1,4,5}

¹*NRC “Kurchatov Institute” - ITEP, 117218 Moscow, Russia*

²*Astronomical Institute, Tohoku University, Aoba-ku, Sendai 980-8578, Japan*

³*Institute for Cosmic Ray Research (ICRR), The University of Tokyo, Tokyo 277-8582, Japan*

⁴*Kavli Institute for the Physics and Mathematics of the Universe (Kavli IPMU, WPI),
The University of Tokyo, Chiba 277-8583, Japan*

⁵*Sternberg Astronomical Institute, Lomonosov Moscow State University, Universitetsky prospekt 13, 119234, Moscow, Russia*

Submitted to ApJ (version closer to published in ApJ)

ABSTRACT

We present nearly self-consistent stellar-halo models of the Fornax dwarf spheroidal galaxy associated with the Milky Way galaxy. Such galaxies are dominated by dark matter and have almost no gas in the system. Therefore, they are excellent objects for N-body modeling that takes into account visible and dark matter halo components. In order to model the dark matter halo inferred from the analysis of the measured velocities of Fornax’s stars, we constructed several self-consistent quasi-equilibrium models based on two source code sets. One of them (GalactICS Software, NEMO) deals with the self-consistent distribution function modeling which depends on energy E and vertical component of the angular momentum L_z . The other is included in the AGAMA framework and is based on Schwarzschild’s calculation of orbits. It can reproduce the non-spherical self-consistent structure of Fornax as the weighted sum of orbit contributions to the galactic density even though the inferred dark halo parameters come from Jeans analysis which does not require that any distribution functions should be positive. To guess the parameters which make the N-body models close to the visible object we use the stellar-dark matter model of the Fornax galaxy based on hydrodynamic axisymmetric Jeans equations taking into account the velocity anisotropy parameter. Then we studied the evolution of the models by performing N-body simulations with the falCON code in order to test their stability. The variability of the model parameters over time was obtained during simulations. The AGAMA models show the best agreement of the resulting velocity dispersion profiles with the observed data.

Keywords: galaxies: dwarf spheroidals – galaxies: kinematics and dynamics – dark matter

1. INTRODUCTION

Dwarf spheroidal (dSph) galaxies associated with the Milky Way (MW) and M31 galaxies are the best probes for studying the properties of dark matter. This is because these galaxies are largely dark matter-dominated objects with dynamical mass-to-light ratios of 10 to 1000 Mateo (1998), Gilmore et al. (2007), McConnachie (2012). Moreover, in the context of bottom-up formation scenarios based on Λ -cold dark matter (Λ CDM) theory, these galaxies are the building blocks of more

massive galaxies, and thus studying their properties and evolution is important to understanding galaxy formation (e.g., Tolstoy et al. 2009).

The hypothesis on the existence of dark matter (DM) was put forward by Zwicky (1933) to explain the virial paradox in the Coma cluster. Later Babcock (1939) found the growth of the rotation curve of M31 in its outer parts and concluded that a large amount of invisible mass was present in it. The hypothesis about DM was revived by Einasto et al. (1974) and Ostriker et al. (1974) in their studies on the rotation curves of galaxies, which appeared to be mostly flat. The flat rotation curves could be artificially explained without DM by the surface density in the disk being inversely proportional to the distance from the center, as established by Mestel

(1963). Nevertheless, the strongest arguments in favor of the existence of DM come from the need to explain the Large-scale structure formation given the small amplitudes of perturbations in the cosmic microwave background radiation (CMB).

Λ CDM theory is a concordance model in modern cosmology that gives an excellent description of the CMB (e.g., Planck Collaboration et al. 2014), large-scale structure (e.g., Tegmark et al. 2004), and the accelerating expansion of the Universe (e.g., Riess et al. 1998). On the other hand, the observational studies on the galactic and sub-galactic scales have turned up several controversial issues that continue to challenge the Λ CDM paradigm. The core-cusp problem is one of the open questions in the Λ CDM picture: the cosmological Λ CDM-based pure dark matter simulations predict that the dark halos on all mass scales have cusped dark matter density profiles. On the other hand, studies of the HI gas rotation curves of low surface brightness galaxies and the stellar kinematics of dwarf galaxies testify in favour of shallower or cored density profiles of galaxies' dark halos (e.g., de Blok et al. 2001; Gilmore et al. 2007).

Another way to explain the lack of visible matter was proposed by Milgrom (1983) who hypothesized that there was a characteristic acceleration below which Newton's law of gravitation was invalid. This is one of the varieties of Modified Gravity (MG) that was subsequently developed, for example, by Bekenstein (2004) and Bekenstein (2010) as the tensor-vector scalar theory, or TeVeS. A variety of MG models has been developed until now (see Casas et al. 2017), but the Λ CDM theory is still the leading paradigm of modern cosmology because the MG is not able to explain the alternative formation paths of the large-scale structure of the Universe as well as the entire set of observations for galaxies and their clusters. For a review, see for example, Read et al. (2019), where different star formation history causes different central DM densities.

Early dark matter study of the Milky Way dSphs was done by Lin & Faber (1983). More recent research can be classified as based on Jeans equations, distribution functions (DFs), action-based DFs, and Schwarzschild's orbit-based methods (for a review see Battaglia et al. 2013). In this work, we focus on Fornax dSph, which is well-studied for its dark matter halo structure. Moreover, this galaxy is suggested to have a core-like dark matter density profile, which behaves like $\rho_{\text{DM}} \sim r^\alpha$, where $\alpha = -0.22$ estimated by Hayashi et al. (2016). Thus, the galaxy can assess the core-cusp problem in the Λ CDM models.

The non self-consistent (stars in the field of DM) spherical Jeans equation approaches were employed taking into account velocity anisotropy for Fornax by Gilmore et al. (2007); Peñarrubia et al. (2008); Strigari et al. (2008); Walker et al. (2009b); Salucci et al. (2012); Read et al. (2019). Axisymmetric models were constructed by Hayashi & Chiba (2012); Hayashi et al. (2016). The DF-based modeling for the stellar component in the field of a parametrized spherical DM potential for Fornax dSph galaxy was done by Wu (2007) and Amorisco & Evans (2011). But all these models are not self-consistent in contrast to the method of Kuijken & Dubinski (1995) who iteratively solved the Poisson equation taking into account the stellar and DM DFs in the common gravitational potential. Their method is realized in the framework of the GALACTICS Software.

Several methods based on the action-based distribution functions have been developed (for a review see Sanders & Binney 2016; Jeffreson et al. 2017, models for globular clusters). The implementation for the Fornax galaxy was done by Pascale et al. (2018), but their models were spherically symmetric.

Schwarzschild's modeling (Schwarzschild 1979; Richstone & Tremaine 1984) was applied to Fornax, Sculptor, Carina and Sextans dSph galaxies by Breddels & Helmi (2013). The non-spherical light distribution in the spherical DM field was taken into account by Jardel & Gebhardt (2012). The spherically symmetric Schwarzschild model of the Fornax dSph galaxy was recently done by Kowalczyk et al. (2019). In this work, we perform two kinds of self-consistent stellar-halo modelings of the Fornax dSph, which are the DF-based one constructed by Kuijken & Dubinski (1995) and the orbit-based one coded within the AGAMA framework (Vasiliev 2018) without assumptions on spherical symmetry. To this end, we utilize the results of the dark matter structures in the Fornax galaxy analyzed by Hayashi & Chiba (2012) and Hayashi et al. (2016). In order to trace the N-body dynamical evolution of our models and to check their self-consistency and stability, we used the code by Dehnen (2002) named falcON.

In this work, we shall find the set of parameters like visible and DM masses, characteristic radii, the radial behaviour of the DM profile near the center and at the periphery. Our goal is to make the modeled dynamical characteristics satisfy the observed ones, such as the velocity dispersion profile. We will perform our investigation in the framework of the standard CDM model. The construction of a feasible evolutionary stable galaxy model is important to find constrains on possible

DM candidates as is shown by [González-Morales et al. \(2017\)](#) and [Safarzadeh & Spergel \(2020\)](#).

2. STELLAR-HALO MODEL

N-body simulations have begun long ago, see [Klypin & Shandarin \(1983\)](#). We construct equilibrium systems (coordinates, masses and velocities of particles) by two methods and then we use the `falcON` code in order to follow the N-body evolution of the systems.

While constructing our systems, we adjust their stellar surface density profiles the observations such as King ([King 1962](#)) or Plummer ([Plummer 1911](#)) profiles. In order to compare our kinematic characteristics to the data, we use the observational velocity dispersion projected onto the line-of-sight profiles done by [Hayashi & Chiba \(2012\)](#) from the data of [Walker et al. \(2009a\)](#).

Our nearly self-consistent stars-halo models of the Fornax galaxy are constructed using the DF-based method of [Kuijken & Dubinski \(1995\)](#) and the orbit-based Schwarzschild’s method by [Vasiliev \(2018\)](#). This is a step forward after previous studies of this object, which were based on the more approximate Jeans equations or spherically symmetric DF or action-based approach. The fitting of the velocity dispersion profile to the data was done only for the mock galaxy by [Vasiliev & Valluri \(2020\)](#) and has not been done for a real astrophysical object. We did not perform the fitting procedure but instead constructed many axisymmetric models with different assumptions about stellar and DM density distributions that satisfy the velocity data rather well. From the set of these models, we pick up one model developed by the `GalaxtICS` Software NEMO code and the other two models by the Schwarzschild’s based code in the AGAMA framework. We report about these models in order to:

- show the best NEMO and AGAMA models (number 1 and 2 in [Table 2](#));
- compare two different approaches and codes (NEMO-model 1 is analogous to AGAMA-model 3);
- study the process of relaxation to equilibrium for different values (NEMO-models are changed more during this process than the AGAMA ones);
- trace the magnitude of change of the previous Jeans velocity dispersion fitting in the field of the axisymmetric prolate DM halo found by [Hayashi et al. \(2016\)](#) (AGAMA model 3).

Table 1. Observed parameters of the Fornax galaxy.

Σ_0	D	r_c	r_t	r_{half}	M
$[L_\odot/\text{pc}^2]$	[kpc]	[']	[']	[kpc]	$[10^6 M_\odot]$
15.7 ± 5.1	147	17.6 ± 0.2	69.1 ± 0.4	0.668	20

NOTE—The central surface brightness (Σ_0) from [Irwin & Hatzidimitriou \(1995\)](#), the distance to the Fornax galaxy (D) from [Pietrzyński et al. \(2009\)](#), the structural parameters (r_c and r_t) for the King formulas 1 from [Battaglia et al. \(2006\)](#), the half-light radius (r_{half}) and luminous mass (M) of the Fornax galaxy from [McConnachie \(2012\)](#).

3. DENSITY MODELS AND PARAMETERS

For the density profile of the stellar component of the galaxy, we use spherically symmetric King (AGAMA model 2 in [Table 2](#)) and axially symmetric Plummer (NEMO model 1 and AGAMA model 3) profiles.

For the King profile, we employ formulas:

$$\rho_{\text{King}}(r) = \begin{cases} \rho_b \left(\frac{1}{\sqrt{1+(r/r_c)^2}} - \frac{1}{\sqrt{1+(r_t/r_c)^2}} \right)^2, & r \leq r_t; \\ 0, & r > r_t, \end{cases} \quad (1)$$

where r is the spherical radial coordinate, ρ_b , r_c and r_t are the central stellar density, the core and tidal radius, respectively. In order to calculate the density parameter ρ_b we use formulas ([B3](#)) in [Appendix B.1](#). We take into account the central surface brightness $\Sigma_0 = 11.0 L_\odot/\text{pc}^2$ and the core and tidal radii as $r_c = 0.53$ kpc, $r_t = 1.66$ kpc. The value of Σ_0 is slightly shifted inside the error bar with respect to the data of [Irwin & Hatzidimitriou \(1995\)](#), and the values of the radii are not inside their error bars (see [table 1](#)), but the best fit overall has been obtained with these values. As we shall see further from [Figure 1](#) this stellar density profile does not differ a lot from the profile of [Irwin & Hatzidimitriou \(1995\)](#).

For the oblate Plummer profile, we use the following function $\rho_{\text{Plummer}}(R, z)$ of the cylindrical coordinates as in [Hayashi et al. \(2016\)](#):

$$\begin{cases} \rho_{\text{Plummer}}(R, z) = \rho_p(m_\star) = \frac{3M_p}{4\pi b_p^3} \left[1 + \frac{m_\star^2}{b_p^2} \right]^{-5/2}, \\ m_\star^2 = R^2 + \frac{z^2}{q^2}, \end{cases} \quad (2)$$

with half-light radius b_p calculated by [Walker et al. \(2010\)](#) as the half surface brightness of the King profile. The same value for the Plummer profile was used

where σ_R is the dispersion of velocity along the cylindrical radius.

Model 2 assumes the visible King profile and the cored DM profile. Its King profile differs slightly from the observed one, but the model has the best reproduction of the velocity dispersion profile (see the Results section). The velocity anisotropy is expressed by the β parameter. Model 3 describes the cusped DM profile and the visible Plummer profile with β_z and κ parameters for the kinematic constrains.

For all our N-body models we used 10^6 stellar particles and 1.5×10^6 DM halo points. For the AGAMA Schwarzschild's orbit-based modeling we used 25000 orbits for each component. For the falcON runs we used all the default parameters except $k_{max} = 6$ ($\tau_{max} = (1/2)^{k_{max}}$) and softening length $\epsilon = 0.1$ (for the code notation see Appendix E).

3.1. DF-based NEMO modeling

For the first sample of our nearly self-consistent stellar-halo modeling (Table 2), we use the bulge and DM components of the NEMO code developed by Kuijken & Dubinski (1995). For the visible component in this code the bulge with King's density profile is used that has the DF described in (Kuijken & Dubinski 1995) by the equation:

$$f_{\text{bulge}}(E) = \begin{cases} \rho_b (2\pi\sigma_b^2)^{-\frac{3}{2}} e^{\frac{\Psi_0 - \Psi_c}{\sigma_b^2}} \left(e^{-\frac{E - \Psi_c}{\sigma_b^2}} - 1 \right) & E < \Psi_c, \\ 0 & E \geq \Psi_c, \end{cases} \quad (9)$$

and the density distribution in a potential Ψ is described by the equation:

$$\rho_{\text{bulge}}(\Psi) = \rho_b \left[e^{\frac{\Psi_0 - \Psi}{\sigma_b^2}} \operatorname{erf} \left(\frac{\sqrt{\Psi_c - \Psi}}{\sigma_b} \right) - \frac{1}{\sqrt{\pi}} e^{\frac{\Psi_0 - \Psi}{\sigma_b^2}} \left(2 \frac{\sqrt{\Psi_c - \Psi}}{\sigma_b} + \frac{4}{3} \frac{(\Psi_c - \Psi)^{\frac{3}{2}}}{\sigma_b^3} \right) \right] \quad (10)$$

This bulge density distribution follows the equipotential surfaces, so it is neither spherical nor ellipsoidal with the given oblateness. It has three parameters: Ψ_c , ρ_b and σ_b .

The DM component construction is based on the lowered Evans distribution Evans & Collett (1993) also described in Kuijken & Dubinski (1995). The DF for DM

is presented as

$$f_{\text{halo}}(E, L_z^2) = \begin{cases} \left[(AL_z^2 + B) e^{-\frac{E}{\sigma_0^2}} + C \right] \left[e^{-\frac{E}{\sigma_0^2}} - 1 \right] & E < 0, \\ 0 & E \geq 0, \end{cases} \quad (11)$$

and the density profile is given by

$$\rho_{\text{halo}}(R, \Psi) = \frac{1}{2} \pi^{\frac{3}{2}} \sigma_0^3 (AR^2 \sigma_0^2 + 2B) \operatorname{erf} \frac{\sqrt{-2\Psi}}{\sigma_0} e^{\frac{-2\Psi}{\sigma_0^2}} + (2\pi)^{\frac{3}{2}} \sigma_0^3 (C - B - AR^2 \sigma_0^2) \operatorname{erf} \frac{\sqrt{-\Psi}}{\sigma_0} e^{\frac{-\Psi}{\sigma_0^2}} + \pi \sqrt{-2\Psi} \left[\sigma_0^2 (3A\sigma_0^2 R^2 + 2B - 4C) + \frac{4}{3} \Psi (2C - A\sigma_0^2 R^2) \right]. \quad (12)$$

Parameters A , B , C are expressed by the velocity and density scales σ_0 and ρ_1 , the halo core radius R_c , and the flattening parameter q as follows (see Kuijken & Dubinski (1994)):

$$A = \frac{8(1-q^2)G\rho_1^2}{\sqrt{\pi}q^2\sigma_0^7} \quad (13)$$

$$B = \frac{4R_c^2 G \rho_1^2}{\sqrt{\pi}q^2\sigma_0^5} \quad (14)$$

$$C = \frac{(2q^2-1)\rho_1}{(2\pi)^{\frac{3}{2}}q^2\sigma_0^3} \quad (15)$$

The density scale ρ_1 is replaced in Kuijken & Dubinski (1995) by R_a :

$$R_a = \left(\frac{3}{2\pi G \rho_1} \right)^{\frac{1}{2}} \sigma_0 e^{\frac{\Psi_0}{2\sigma_0^2}} \quad (16)$$

For the DM NEMO model we need 5 parameters:

- q – axial ratio, an optional flattening parameter for the potential ;
- Ψ_0 – central potential;
- $v_0 = \sqrt{2} \times \sigma_0$, where σ_0 is the central velocity dispersion;
- R_a – the radius at which the halo rotation curve, if continued at its $r = 0$ slope, would reach the value $\sqrt{2}\sigma_0$, a scaling radius for the halo;
- $r_{ck}^2 = \frac{R_c^2}{R_K^2}$ – a core smoothing parameter – the ratio of the core radius (R_c) to the derived King radius (R_K). This is the radius at which the gravitational potential has risen by about $2\sigma_0^2$ over its central value, provided that the potential well depth is above $2\sigma_0^2$.

Figure 1. Initial bulge density distribution for model 1 and different visible density profiles see sec. 3.1 for details.

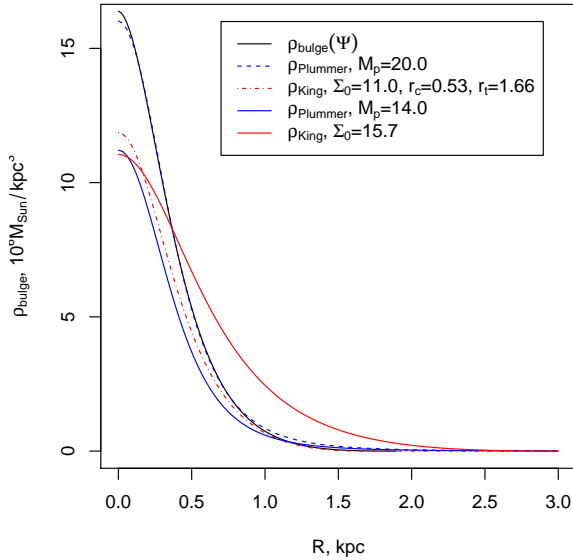
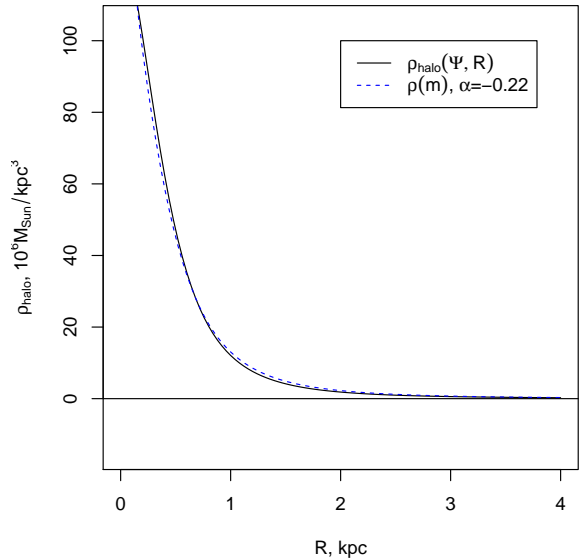


Figure 2. Initial halo density distribution for model 1 and Hayashi et al. (2016) DM density profile.



For the bulge NEMO model which stands for our visible part of the galaxy we need 3 parameters:

- ρ_b – central density;
- Ψ_c – bulge cut-off potential;
- σ_b – bulge central potential.

The names of parameters for mkkd95 code can be found in the table 9 in the Appendix.

First we relied on the density distributions of the components mentioned in the previous section (the density distribution, eq. (1), for the visible part, and eq. (4) for the DM part of the galaxy) to calculate parameters v_0 , R_a , r_{ck}^2 , ρ_b , Ψ_c , σ_b . With this approach we failed to construct the NEMO-model by the mkkd95 code. The next idea was to fit the density distributions (eqs. 10 and 12) directly to the density distributions (eqs. 2 and 4). To do this, we need an initial guess on the distribution of the potential derived from our density distributions. We have calculated the combined potential distribution $\Psi(R, z = 0)$ in cylindrical coordinates in the equatorial plane $z = 0$ (see the Appendix).

For the first model we need to find the central potential Ψ_0 as the sum of the central prolate DM potential and the central stellar potential. For calculating central DM potential we use eq. (D42) for the case $r = 0, z = 0$. As the μ function for this formula we used eq. (C12) for the prolate cusped Zhao DM potential. For the Plummer oblate central stellar potential we used eq. (C8).

After that we do the fitting procedure for the function eq. (10) (with known Ψ_0 and three free parameters Ψ_c , σ_b and ρ_b) to the Plummer density distribution function eq. (2). To do this we need to numerically integrate eq. (D44), the same as eq. (C6) as the growth of the DM potential over its central value. We also need to get the limit of the formula for the stellar eq. (C8) radial potential distribution at the equatorial plane of the galaxy. (We use the value $x = 10000$ instead of ∞ .)

In Figure 1 the fitted function $\rho_{\text{bulge}}(\Psi)$ from eq. (10), shown by the black line, almost coincides with the data curve ρ_{Plummer} with $M_p = 20.0$ parameter from eq. (2), depicted by the blue dash-line. This value of the parameter makes the stellar density profile as the one taken by Hayashi et al. (2016). This profile was also assumed when constructing the AGAMA model 3. The red dash-dotted line represents the King profile taken for the AGAMA model 2. This profile lies near the Plummer density profile shown by the blue solid line with the stellar mass $\sim 20.0 \times 10^6 M_\odot$ from McConnachie (2012) and $M_p = 14.0$ parameter. The stellar profile for model 2 lies also near the King profile given by Irwin & Hatzidimitriou (1995) shown by the red solid line.

The next step is fitting the function eq. (12) with three free parameters σ_0 , B and C to the DM density distribution function eq. (4). In Figure 2 the fitted function $\rho_{\text{halo}}(\Psi, R)$ from eq. (12), shown by the black line, almost coincides with the DM density profile

Table 4. Parameters for NEMO models.

Model	ρ_b	ψ_c	σ_b	q	Ψ_0	v_0	R_a	r_{ck}^2	Δ
1	20.75	-277.5	7.796	1.11	-494.6	14.97	642.5	$1.3 * 10^{11}$	11.8%

$\rho(m)$ from Hayashi et al. (2016) (see eq. 4). This curve is shown by the blue dash-line. Then we get v_0 from σ_0 and R_a value from those parameters using the expression in eq. (16). To find the r_{ck}^2 value we need to calculate R_c using eqs. (14, 15) and R_K . This value is the radius at which the rise of the combined potential over its central value is equal to $2\sigma_0^2$.

The fitting procedures were done for the density distributions at the equatorial plane of the galaxy. By these two fits we have gotten 5 parameters for the mkkd95 NEMO modeling listed in Table 4.

The parameters taken from the fitting procedures (Table 4) are the initial parameters for the NEMO-modeling. We can also see a variable Δ in Table 4 which is a measure of the violation of the virial theorem at the initial point of the numerical falCON evolution of the constructed galaxy model, namely, $\Delta = -(2T/W) - 1$, where T is the kinetic energy and $W < 0$ is the potential energy of the system.

3.2. Orbit-based AGAMA modeling

The AGAMA framework developed by Vasiliev (2018) is able to form an orbit-based model from some specific and common patterns of densities and DFs.

For the DM halo we use the Spheroid AGAMA component of the following form:

$$\rho(\bar{r}) = \rho_0 \left(\frac{\bar{r}}{b_{\text{halo}}} \right)^\alpha \left[1 + \left(\frac{\bar{r}}{b_{\text{halo}}} \right)^{-\gamma} \right]^{\frac{-\alpha-\eta}{\gamma}} \times \exp \left[- \left(\frac{\bar{r}}{r_{\text{cut}}} \right)^\xi \right], \quad \bar{r} = \sqrt{x^2 + (y/p)^2 + (z/Q)^2}. \quad (17)$$

Far from the r_{cut} radius the above form coincides with the DM profile (eq. 4) when

$$\gamma = 2, \quad \eta = 3, \quad p = 1.0. \quad (18)$$

For all models we set $\eta = 3$, and $\gamma = 2.0$ (see table 5). As for the r_{cut} and ξ parameters we use the following numbers for all our AGAMA models:

$$r_{\text{cut}} = 55, \quad \xi = 2.5. \quad (19)$$

The visible component is set either by the Plummer or King density profiles. To construct the Plummer component using the orbit-based AGAMA code we need the

Table 5. Parameters for AGAMA DM component.

Model	ρ_0	b_{halo}	γ	α	Q
2	87.1	0.617	2.0	0.0	1.11
3	87.1	0.617	2.0	-0.22	1.11

Table 6. Parameters for AGAMA visible component.

Model	M_{stars}	r_{cA}	W_0	β	β_z	κ
King Visible component						
2	12.13	0.753	1.786	-0.17	-	-
Plummer visible component						
		b_p	q			
3	13.19	0.668	0.66	-	0.47	1.0

parameters Q, p, b_p , and M_{stars} for the total component mass parameter. Taking into account the formulas C10 from the Appendix we can estimate this mass from the M_p parameter:

$$M_{\text{stars}} = qM_p. \quad (20)$$

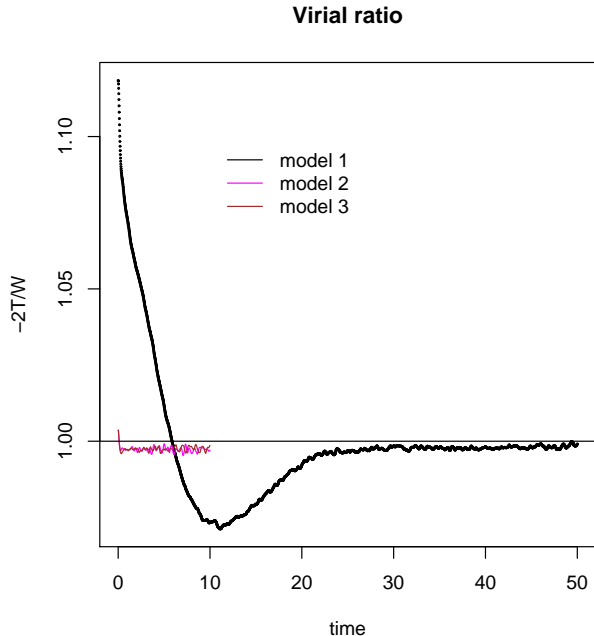
For the King component we need M_{stars}, r_{cA} and $W_0 = [\Psi(r_t) - \Psi(0)]/\sigma^2$ parameters. The latter is the dimensionless potential depth of the generalized King (lowered isothermal) models (see AGAMA documentation). The identifiers of parameters for the AGAMA Schwarzschild's code can be found in Table 10 in the Appendix.

We have gotten two AGAMA models, one of them having the cusped DM density profile as Hayashi et al. (2016).

The first AGAMA model 2 assumes the visible density King profile with the velocity anisotropy $\beta = -0.17$. The characteristic radius and density for the halo component are from Hayashi et al. (2016) but the profile is cored. The second AGAMA model 3 employs the Plummer visible density profile and more appropriate velocity anisotropy parameters for the model of Hayashi et al. (2016) and the same parameters for the DM component.

Figure 3. Evolution of the virial ratio

One time unit corresponds to 0.47 Gyr (see eq. 5). NEMO and AGAMA models are depicted all together. AGAMA lines merge to one multicolored curve after about 10 time units. In contrast to NEMO model, there is no sense to follow the AGAMA evolution further.



4. RESULTS

Figure 3 demonstrates that orbit-based AGAMA code produces the systems which are in much better equilibrium than the ones from the mkkd95 NEMO code. The falcON code computes the virial ratio for each step of system evolution. The values of this ratio for all our models over the time evolution steps are depicted in Figure 3. We can see that the AGAMA values Δ for the violation of the virial theorem (models 2–3) are negligible in comparison to the ones for the NEMO model.

From this figure, all of models reach to the equilibrium sooner or later.

4.1. NEMO modeling

The Dehnen (2002) manipulators for the N-body galaxy snapshot files are able to calculate the profiles of different physical quantities averaged either over the spherical radius or over the cylindrical radius. In the latter case we use the projection along the line-of-sight. Figure 4 shows the evolution of modeled surface density profiles of the visible and DM components and the initial analytical profiles. There are several analytical profiles of the surface density along different axes and the averaged surface density.

We also found the best-fit parameters of the King distribution for time $t = 0.4$ modelled profile. The fitting dash-dotted line is hidden by orange, red and brown symbols standing for $t = 0.3$, $t = 0.4$ and $t = 10$ density profiles. The parameters for the line are included in the legend of Figure 4.

For the model we can see that the stellar surface density profile (in the left panel of Figure 4) falls down by about 20% at the first evolution steps and then fluctuates about its equilibrium position. This falling is a factor of two faster than the falling of the other our NEMO models not presented here. But this model shows the best agreement with the velocity dispersion data among all our NEMO models.

Earlier than $t \sim 10.0$ the virial ratio does not reach its equilibrium value (Figure 3) but we can say that all further fluctuations of projected profiles lie between $t = 0.1$ and $t = 0.4$ lines.

In the right panels of Figure 4, we can see smaller relative drop of the surface density during the first evolution steps in comparison with the visible density profile.

We can compare modelled velocity dispersion projected onto the line-of-sight and averaged over the cylindrical radius of the sky plane profile and its falcON evolution directly to the observational velocity dispersion points. We need to multiply projprof Dehnen manipulator velocity data by $V_{\text{scale}} = 2.079$ in order to convert $\sqrt{10^6 M_{\odot}/\text{kpc}}$ velocity units to km/s.

We use χ^2 test to compare our models:

$$\chi^2 = \sum_{i=1}^N \frac{(\sigma_l(R_{\text{obs}}^i) - (\sigma_{\text{obs}}^i))^2}{(\delta\sigma_{\text{obs}}^i)^2}, \quad (21)$$

where $\sigma_l(R_{\text{obs}}^i)$ are mean modelled velocity dispersions projected to the line-of-sight over the modelled star points spaced R_{obs}^i apart the line-of-sight axis, σ_{obs}^i are the observational velocity dispersions at R_{obs}^i radii and $\delta\sigma_{\text{obs}}^i$ are observational errors.

We do not perform the fitting procedure for minimizing χ^2 by varying parameters because each set of the parameters stands for one 10^6 particles N-body simulation so fitting procedure would take too many computational resources. That is why we use hydrodynamical parameters to start our modeling. The mean value of χ^2 averaged over time for $t \geq 0.35$ is 83.5 for model 1. In the Appendix A.1 we discuss the time interval for averaging and the equilibrium velocity dispersion profile which becomes so much earlier than the Δ parameter does. Figure 5 represents the velocity dispersion projected to the line-of-sight profile for several evolution time points of the falcON in comparison to the observational data with error bars.

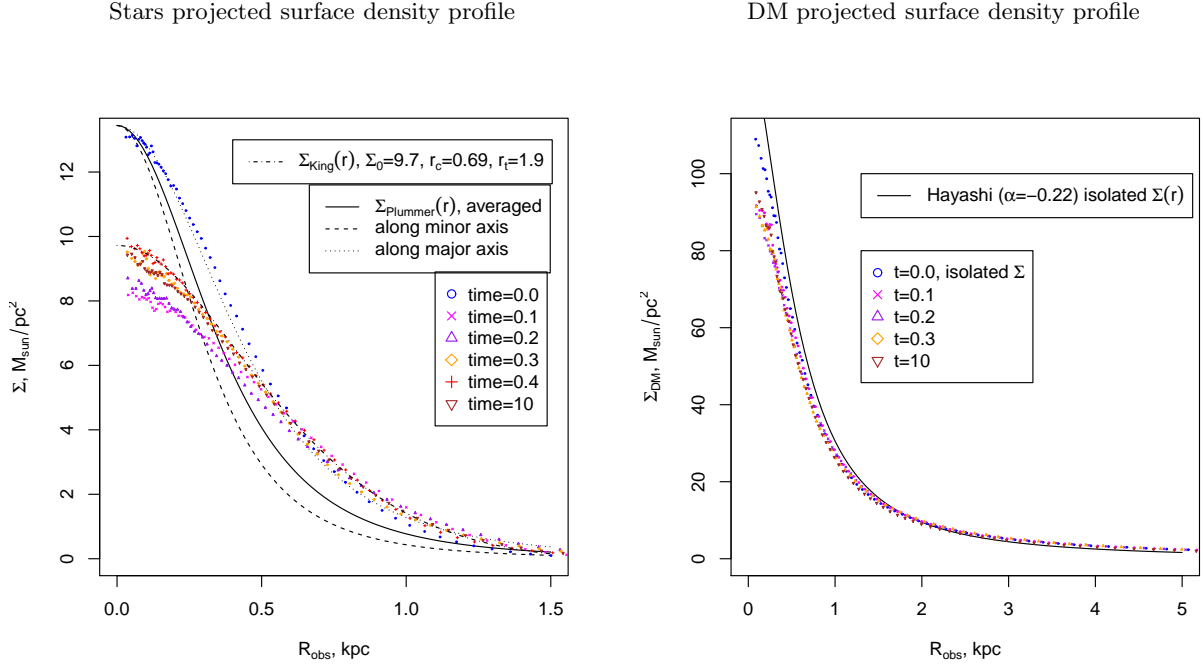


Figure 4. Surface density evolution of components for NEMO model

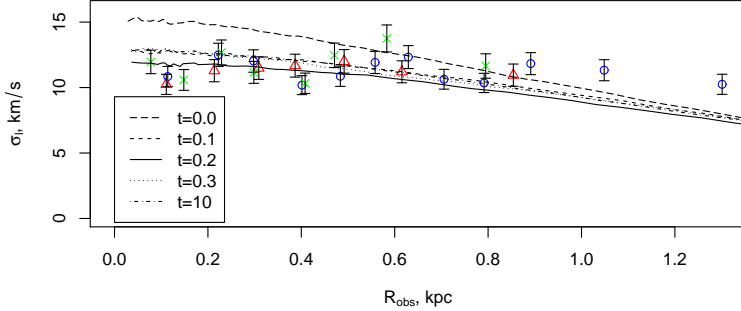


Figure 5. NEMO model vs observed stars velocity dispersion profile

The blue circles represent data measured along the major galaxy axis, the red triangles represent data measured along the minor axis, and the green crosses represent data measured along the middle axis.

4.2. AGAMA modeling

The AGAMA modeled visible and DM surface density profiles are depicted in the figure 6. We can see the decrease of stellar surface density profile for the equilibrium establishing time interval. And such decreasing in the central part of the galaxy is less than that for the NEMO model 1.

But in contrast to this model the changing of density profiles over time for the AGAMA systems is noticeable only at the central part of the galaxy with $r \lesssim 0.25$ kpc. For the NEMO model the radius of noticeable change of the surface density profile is not less than 0.5 kpc.

For model 2 we found Σ_0, r_c, r_t King profile parameters that fit well the start surface density profile with the initial W_0, r_c and M_{stars} AGAMA parameters. They are shown on the panel for this model in the figure 6.

For model 3 we depicted the averaged Plummer surface density profile as a black line taking into account our start parameters.

The second row of Figure 6 is shown by the DM surface density profiles. All the initial profiles almost coincide with the analytical profiles taking our initial parameters. We can also see small evolution changes of these profiles.

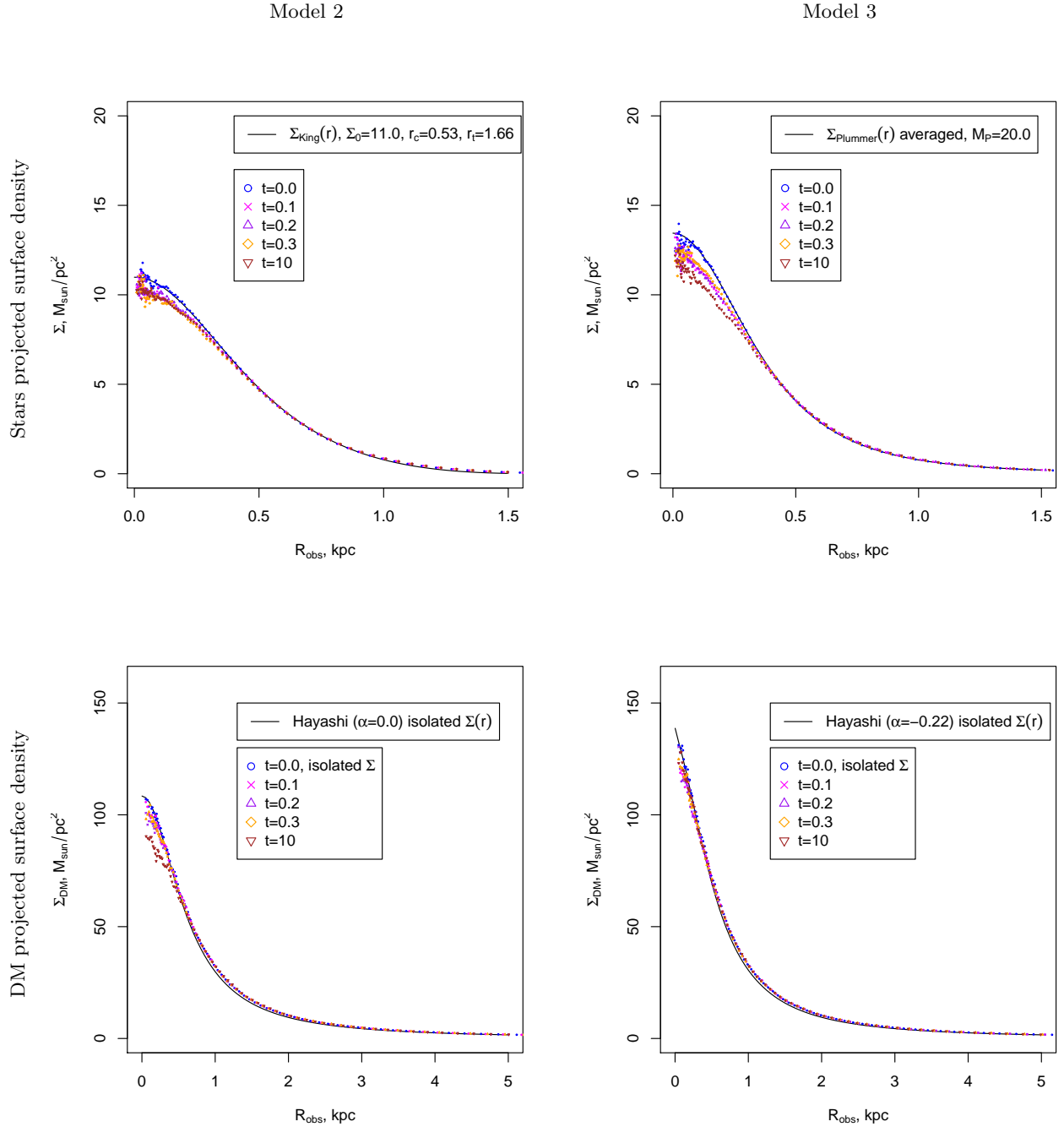


Figure 6. Surface density evolution of components for AGAMA models

The greatest change for model 2 is less than the smallest one for our NEMO model.

Model 3 has almost the same initial parameters as the NEMO-model 1 which coincides with the [Hayashi et al. \(2016\)](#) parameters. Model 3 changes less than the corresponding NEMO-model but the ensuing evolution curves of the model 1 intersect more data error bars than those of the AGAMA model.

Table 7. Mean values of χ^2

	1	2	3
$\overline{\chi^2}$	83.5	36.5	104.7

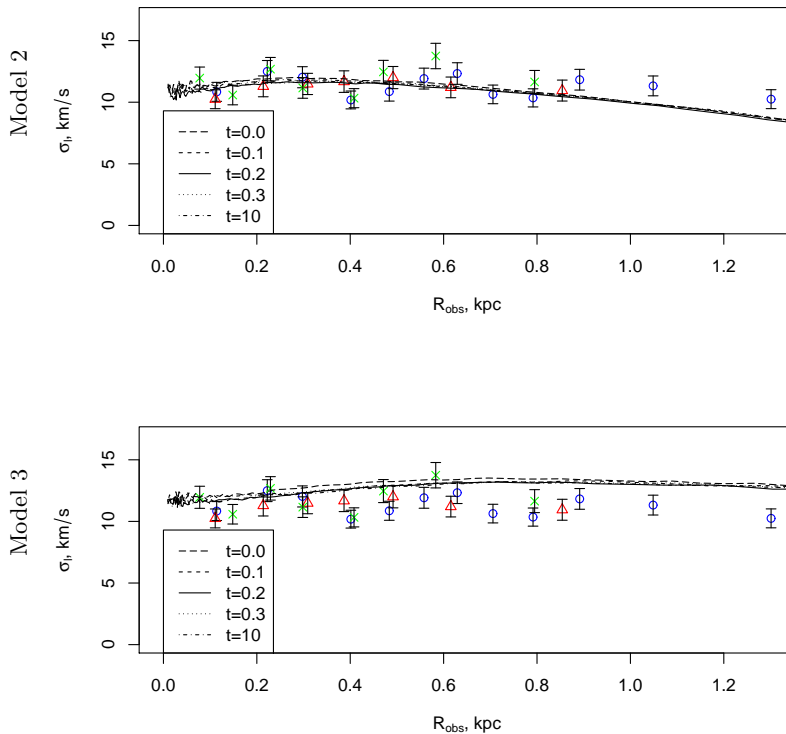


Figure 7. AGAMA models vs observed stars velocity dispersion profiles

We can see the averaged values of χ^2 over time for $t \geq 0.2$ for the AGAMA models and for $t \geq 0.35$ for the NEMO model in Table 7. In the Appendix A.2 the discussion about this averaging can be found. The mean equilibrium χ^2 value for the NEMO model 1 is less than that of the AGAMA model 3.

The worst χ^2 is for model 3 with $\alpha = -0.22$ and $\beta_z = 0.47$. It seems that this galaxy shows better cored DM profile. Among the multitude of our other models we can say that exact Hayashi et al. (2016) profile is better with $\beta_z = 0.47$ velocity anisotropy parameter and $\alpha = 0.0$ or $\gamma = 1.0$ DM profiles are better with $\beta_z = -0.17$ or $\beta = -0.17$ parameters.

In Figure 7 we can see that the AGAMA models are compliant with the observational data with different form of curves. Notation of the points is the same as in Figure 5.

Let us compare the best NEMO and AGAMA models stellar component equilibrium profiles. The King parameters for them are listed in Table 8. We can see that for both models Σ_0 is on the bottom edge of the observed error bar or a bit lower. The structural parameters are closer to the Battaglia et al. (2006) data.

5. COMPARISON WITH PREVIOUS WORK

Table 8. King best-fit parameters vs observations.

	$\Sigma_0, L_\odot/\text{pc}^2$	r_c, kpc	r_t, kpc
observed 1	15.7 ± 5.1	0.75 ± 0.01	2.95 ± 0.02
observed 2	15.7 ± 5.1	0.58 ± 0.05	3.04 ± 0.17
model 1	9.7	0.69	1.9
model 2	11.0	0.53	1.66

NOTE— Fitted to observation structural parameters from Battaglia et al. (2006) – observed 1; Irwin & Hatzidimitriou (1995) – observed 2.

Let us compare our results with the investigations of Pascale et al. (2018), Amorisco & Evans (2011) and Strigari et al. (2008). We can estimate the dynamical mass $M_{\text{dyn}}(r)$ of our best model inside the spheres of 1.05 kpc and 300 pc radii.

For $M_{\text{dyn}}(1.05 \text{ kpc})$ we have $1.29 \times 10^8 M_\odot$ for our model 2. The estimation of Pascale et al. (2018) for this mass is $1.38 \pm 0.10 \times 10^8 M_\odot$ compared with the estimation of Amorisco & Evans (2011) at $1.3 \times 10^8 M_\odot$. We can see that our numbers are consistent with the previous results.

The mass enclosed in a sphere of 300 pc radius is $0.93 \times 10^7 M_\odot$ for model 2. The results of Strigari et al. (2008) for $M_{\text{dyn}}(0.3\text{kpc})$ is $1.14_{-0.12}^{+0.09} \times 10^7 M_\odot$. Smaller value at $0.44_{-0.03}^{+0.07} \times 10^7 M_\odot$ is the estimation of Pascale et al. (2018). We can see that our numbers for a smaller radius is closer to the older estimations of Strigari et al. (2008).

We can also compare our results to the DM halo density at 150 pc radius modeled by Read et al. (2019) by their GravSphere code based on the spherical Jeans equations and their sophisticated assumptions about the **velocity** anisotropy parameter. They obtained the value $\rho_{\text{DM}}(150 \text{ pc}) = 0.79_{-0.19}^{+0.27} \times 10^8 M_\odot/\text{kpc}^3$. The values of this density for all our models are inside this error bar. We can say that our results are also **consistent** with the estimations of Read et al. (2019).

6. CONCLUSION

The main point of this paper is that we first investigate whether the dynamical non-spherical structure of Fornax dSph estimated from kinematic analysis by (Hayashi et al. 2016) is stable or not. We have constructed the N-body models by two source codes for the Fornax galaxy from these hydrodynamical studies and followed their numerical evolution.

Then we found that the AGAMA model with the inferred dark halo parameters demonstrates that indeed, such a system may be stable during several dynamical times.

Both methods (NEMO and AGAMA) used in our paper give approximate realizations of stationary models. AGAMA is much more accurate, which is clear from the criterion of virial test. Moreover, AGAMA can reproduce the non-spherical self-consistent structure of Fornax as the weighted sum of orbit contributions to the galactic density even though the inferred dark halo parameters come from Jeans analysis which does not require that any distribution functions should be positive.

We have also changed some assumptions about the stellar and DM density distributions and got the model that fits the kinematical data much better than the models found in previous studies. Better DM profiles are

cored profiles. The velocity anisotropy parameter for the stellar component also shows some correlations with the DM profile characteristics. The best stellar profile is the King profile. We choose this model in favour of the best agreement with the velocity dispersion data than with the luminosity data because the velocity dispersion observations are more precise than the luminosity ones.

One should understand that even exactly stationary DF-based models may be dynamically or secularly unstable (there are numerous well-known stationary solutions for collisionless disk-like or ellipsoidal systems which may be unstable). Thus, N-body evolution is needed to test not only the deviations from the exact stationary solution but also to check the stability. Our results provided by falcON simulations do show that all our models are dynamically stable since they support their shapes with small oscillations for several dynamical time-scales.

Using N-body simulation results, one can confine the prior distributions of dark matter halo parameters such as scale radius and scale density. Based on observational results (such as Jeans analysis by Hayashi et al. 2016) our analysis, applied to other dwarf galaxies, can obtain the limits on the parameter ranges of the dark matter halo which sustain dynamical equilibrium. Therefore, using the confined parameter ranges, we may improve the limits on the nature of DM particle through its annihilation (Ando et al. 2020).

ACKNOWLEDGEMENTS

The authors are grateful to Eugene Vasiliev for his invaluable help with the AGAMA code and to Marat Potashov for debugging FalcOn code.

We are grateful to the anonymous referee for useful comments which helped us to improve the presentation of our results.

This work was supported by JSPS KAKENHI Grant Numbers, 18H04359 & 18J00277 for K.H.

S.B. is grateful to Sternberg Astronomical Institute, MSU, for generous support.

REFERENCES

- Amorisco, N. C., & Evans, N. W. 2011, MNRAS, 411, 2118
 Ando, S., Geringer-Sameth, A., Hiroshima, N., et al. 2020, PhRvD, 102, 061302
 Babcock, H. W. 1939, Lick Observatory Bulletin, 498, 41
 Battaglia, G., Helmi, A., & Breddels, M. 2013, NewAR, 57, 52
 Battaglia, G., Tolstoy, E., Helmi, A., et al. 2006, A&A, 459, 423
 Bekenstein, J. D. 2004, PhRvD, 70, 083509
 —. 2010, Modified gravity as an alternative to dark matter, ed. G. Bertone, 99
 Binney, J., & Tremaine, S. 2008, Galactic Dynamics: Second Edition (Princeton University Press)
 Breddels, M. A., & Helmi, A. 2013, A&A, 558, A35
 Casas, S., Kunz, M., Martinelli, M., & Pettorino, V. 2017, Physics of the Dark Universe, 18, 73

- de Blok, W. J. G., McGaugh, S. S., Bosma, A., & Rubin, V. C. 2001, *ApJ*, 552, L23
- Dehnen, W. 2002, *Journal of Computational Physics*, 179, 27
- Einasto, J., Kaasik, A., & Saar, E. 1974, *Nature*, 250, 309
- Evans, N. W., & Collett, J. L. 1993, *MNRAS*, 264, 353
- Gilmore, G., Wilkinson, M. I., Wyse, R. F. G., et al. 2007, *ApJ*, 663, 948
- González-Morales, A. X., Marsh, D. J. E., Peñarrubia, J., & Ureña-López, L. A. 2017, *MNRAS*, 472, 1346
- Hayashi, K., & Chiba, M. 2012, *ApJ*, 755, 145
- . 2015, *ApJ*, 810, 22
- Hayashi, K., Ichikawa, K., Matsumoto, S., et al. 2016, *MNRAS*, 461, 2914
- Irwin, M., & Hatzidimitriou, D. 1995, *MNRAS*, 277, 1354
- Jardel, J. R., & Gebhardt, K. 2012, *ApJ*, 746, 89
- Jeffreson, S. M. R., Sanders, J. L., Evans, N. W., et al. 2017, *MNRAS*, 469, 4740
- King, I. 1962, *AJ*, 67, 471
- Klypin, A. A., & Shandarin, S. F. 1983, *MNRAS*, 204, 891
- Kowalczyk, K., del Pino, A., Lokas, E. L., & Valluri, M. 2019, *MNRAS*, 482, 5241
- Kuijken, K., & Dubinski, J. 1994, *MNRAS*, 269, 13
- . 1995, *MNRAS*, 277, 1341
- Lin, D. N. C., & Faber, S. M. 1983, *ApJL*, 266, L21
- Mateo, M. L. 1998, *Annual Review of Astronomy and Astrophysics*, 36, 435
- McConnachie, A. W. 2012, *AJ*, 144, 4
- Mestel, L. 1963, *MNRAS*, 126, 553
- Milgrom, M. 1983, *ApJ*, 270, 365
- Ostriker, J. P., Peebles, P. J. E., & Yahil, A. 1974, *ApJ*, 193, L1
- Pascale, R., Posti, L., Nipoti, C., & Binney, J. 2018, *MNRAS*, 480, 927
- Peñarrubia, J., McConnachie, A. W., & Navarro, J. F. 2008, *ApJ*, 672, 904
- Pietrzyński, G., Górski, M., Gieren, W., et al. 2009, *AJ*, 138, 459
- Planck Collaboration, Ade, P. A. R., Aghanim, N., et al. 2014, *A&A*, 571, A16
- Plummer, H. C. 1911, *MNRAS*, 71, 460
- Read, J. I., Walker, M. G., & Steger, P. 2019, *MNRAS*, 484, 1401
- Richstone, D. O., & Tremaine, S. 1984, *ApJ*, 286, 27
- Riess, A. G., Filippenko, A. V., Challis, P., et al. 1998, *AJ*, 116, 1009
- Safarzadeh, M., & Spergel, D. N. 2020, *ApJ*, 893, 21
- Salucci, P., Wilkinson, M. I., Walker, M. G., et al. 2012, *MNRAS*, 420, 2034
- Sanders, J. L., & Binney, J. 2016, *MNRAS*, 457, 2107
- Schwarzschild, M. 1979, *ApJ*, 232, 236
- Strigari, L. E., Bullock, J. S., Kaplinghat, M., et al. 2008, *Nature*, 454, 1096
- Tegmark, M., Blanton, M. R., Strauss, M. A., et al. 2004, *ApJ*, 606, 702
- Tolstoy, E., Hill, V., & Tosi, M. 2009, *Annual Review of Astronomy and Astrophysics*, 47, 371
- Vasiliev, E. 2018, *MNRAS*, 2556
- Vasiliev, E., & Valluri, M. 2020, *ApJ*, 889, 39
- Walker, M. G., Mateo, M., & Olszewski, E. W. 2009a, *AJ*, 137, 3100
- Walker, M. G., Mateo, M., Olszewski, E. W., et al. 2009b, *ApJ*, 704, 1274
- . 2010, *ApJ*, 710, 886
- Wu, X. 2007, arXiv e-prints, astro
- Zhao, H. 1996, *MNRAS*, 278, 488
- Zwicky, F. 1933, *Helvetica Physica Acta*, 6, 110

Figure 8. Models velocity dispersion χ^2 . Horizontal lines are the mean values of χ^2 for times $t \geq 0.35$ for NEMO model 1 and for times $t \geq 0.2$ for AGAMA models 2 and 3.

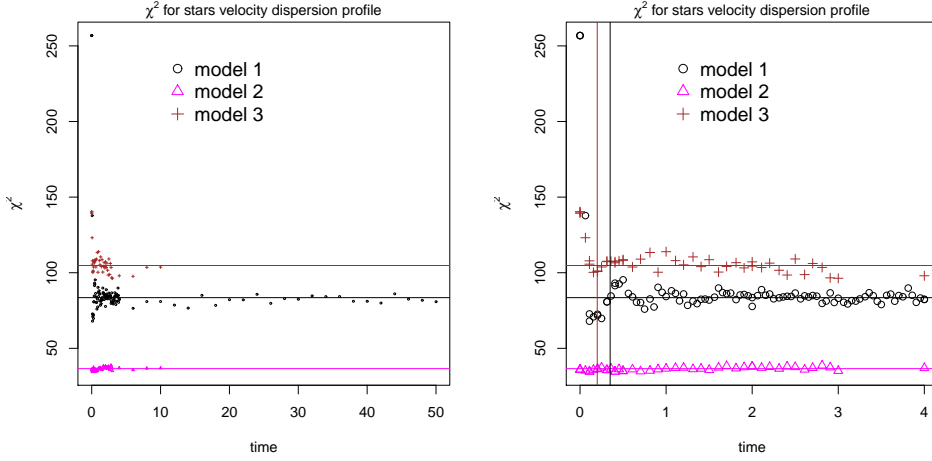
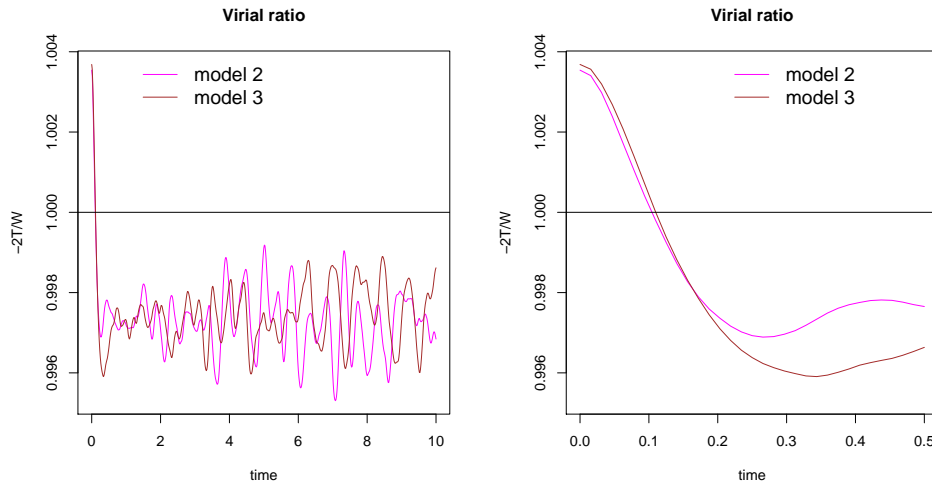


Figure 9. Evolution of the virial ratio for AGAMA models



APPENDIX

A. MORE DETAILS ABOUT THE MODELING RESULTS

A.1. NEMO results

In Figure 8 variations of the χ^2 values over time are depicted. We can see how the χ^2 moves towards its equilibrium value for NEMO model 1 for times $t < 4$ in the right panel of Figure 8. This equilibrium value of χ^2 can be estimated as the mean values for times about $t \geq 0.35$ and is depicted as horizontal black line in Figure 8. The estimations are included in Table 8. We can see that the χ^2 quantity starts to oscillate over its equilibrium value much more earlier than the Δ quantity (see Figure 3), so we choose this time interval for averaging of χ^2 for the NEMO model.

A.2. AGAMA results

Let us consider in detail the equilibrium characteristics of our AGAMA models. Their virial ratio evolution is depicted in Figure 9. We can see that the absolute magnitude of Δ start values are not greater than their following evolution

values in contrast to our NEMO model. But the sign of violation for all our N-body systems starts from positive one tending to negative value during the first time interval of the evolution, see Figure 9. In terms of equilibrium all our AGAMA models are equally good.

Let us look at the evolution of the χ^2 values for the models 2–3 in Figure 8 in order to compare their accordance with the data. In the right panel of Figure 8 we can see the initial steps of the χ^2 evolution. The setting of equilibrium is completed by the time $t = 0.2$ (see brown vertical line) for model 3 and is not resolved for model 2. So in Figure 8 the lines for the mean values of χ^2 after $t = 0.2$ for models 2 and 3 are depicted. We find that the best model with the lowest χ^2 is model 2 with the core DM density profile and the King best-fit stellar component parameters.

B. KING DISTRIBUTION

In this appendix we give a summary of a usefull formulas for the King (1962) distribution which are not easily find in the textbook.

B.1. Central surface density of the King's distribution

Now we shall express characteristic density ρ_b in terms of observed quantities r_c, t and Σ_0 – central surface density of the Fornax galaxy. Then we are to find the expression of Σ_0 for the King's distribution:

$$\Sigma_0 \equiv 2 \int_0^{r_c} \rho_{\text{King}}(r) dr \equiv 2\rho_b r_c s_0(t), \quad (\text{B1})$$

where

$$s_0(t) = \arctan t - \frac{2 \log(t + \sqrt{t^2 + 1})}{\sqrt{t^2 + 1}} + \frac{t}{t^2 + 1}. \quad (\text{B2})$$

For the characteristic density ρ_b expressed in terms of r_c, t, Σ_0 we get:

$$\rho_b = \frac{\Sigma_0}{2r_c s_0(t)}. \quad (\text{B3})$$

C. GRAVITATIONAL POTENTIAL FROM AXISYMMETRIC DENSITY DISTRIBUTION (OBLATE SYSTEMS)

In this appendix we cite some formulae from Binney & Tremaine (2008) in order to write down equations for the radial distribution of the potential at the equatorial plane for the Plummer oblate density profile and DM oblate density profiles. The latter formulae are usefull for the radial distribution of the potential for the prolate DM density profiles. We need these distributions for fitting NEMO code input parameters.

Let us consider gravitational system with equidensity axisymmetric ellipsoids of ellipticity e and axial ratio Q . Then for our parameter we take m , so, that for cylindrical coordinates of equidensity ellipsoid (R, z) we have equation:

$$m^2 = R^2 + z^2/Q^2, \quad Q^2 = 1 - e^2. \quad (\text{C4})$$

Then we can define density as a function of m , $\rho(m)$, and define function $\mu(m)$ as:

$$\mu(m) = \int_0^m \rho(\bar{m}^2) d(\bar{m}^2). \quad (\text{C5})$$

Then from Binney & Tremaine (2008) we have a formula for gravitational potential $\Psi(R_0, z_0)$ of such systems. Let us write down the rise of the potential over its central value in terms of Q instead of e :

$$\Psi(R_0, z_0) - \Psi(0, 0) = \pi G Q a_0 \int_0^\infty \frac{\mu(m) d\tau}{(\tau + a_0^2) \sqrt{\tau + b_0^2}},$$

where τ is defined by the equation: $\frac{R_0^2}{\tau + a_0^2} + \frac{z_0^2}{\tau + b_0^2} = \frac{m^2}{a_0^2}, \quad b_0 = Q a_0. \quad (\text{C6})$

C.1. Plummer potential distribution at the equatorial plane

Let's find potential of the prolate Plummer distribution (2):

$$\begin{cases} \rho_{\text{Plummer}}(R, z) = \rho_p(m_\star) = \frac{3M_p}{4\pi b_p^3} \left[1 + \frac{m_\star^2}{b_p^2}\right]^{-5/2}, \\ m_\star^2 = R^2 + \frac{z^2}{q^2}, \end{cases}$$

with the oblateness q and ellipticity $e = \sqrt{1 - q^2}$. Then the function μ from (C5) for this profile will be:

$$\mu(m) = \frac{M_p}{2\pi b_p} \left(1 - \frac{1}{(1 + m^2/b_p^2)^{3/2}}\right). \quad (\text{C7})$$

Let's find the potential distribution at the equatorial plane for $z_0 = 0$:

$$\Psi(R_0, 0, 0) = -\frac{M_p G q}{b_p \sqrt{1 - q^2}} \times \left(\frac{x}{(k+1)^{3/2}} F_1 \left(\frac{1}{2}; -\frac{1}{2}; \frac{3}{2}; \frac{3}{2}; -x^2; -\frac{x^2}{k+1} \right) \right) \Big|_{q/e}^{\infty}, \quad (\text{C8})$$

where F_1 is Gauss hypergeometric function.

C.2. Plummer mass for the oblate system

In order to calculate the mass of such a system we shall use formulae for mass of a thin homeoid between ellipsoids with oblateness q and equatorial radii m and $m + dm$ from Binney & Tremaine (2008):

$$\delta M = 4\pi \rho(m_\star) m_\star^2 q dm. \quad (\text{C9})$$

Then the mass inside such an ellipsoid will be equal to:

$$M(m_\star) = 4\pi q \int_0^{m_\star} \rho(\tilde{m}) \tilde{m}^2 d\tilde{m} = q M_p \frac{m^3}{(b_p^2 + m^2)^{3/2}}. \quad (\text{C10})$$

C.3. Zhao density distribution with one parameter

Let us consider Hayashi et al. (2016) density distribution of the DM halo. More common form of such a DM profile we can find at Zhao (1996). We shall rewrite the function $\rho(m)$ from equation (4) in terms of variable $p = m/b_{\text{halo}}$:

$$\rho(p) = \rho_0 p^\alpha (1 + p^2)^{-(\alpha+3)/2}, \quad p = \frac{m}{b_{\text{halo}}}, \quad \tilde{p} = \frac{\tilde{m}}{b_{\text{halo}}}; \quad (\text{C11})$$

and calculate function $\mu(m)$ for our density distribution:

$$\mu(m) = \frac{\rho_0 b_{\text{halo}}^2}{\frac{\alpha}{2} + 1} \tilde{p}^{\alpha+2} {}_2F_1 \left(\frac{\alpha}{2} + 1, \frac{\alpha}{2} + 1.5, \frac{\alpha}{2} + 2, -\tilde{p}^2 \right) \Big|_0^{\frac{m}{b_{\text{halo}}}}, \quad (\text{C12})$$

where ${}_2F_1(a, b, c, z)$ is Gauss hypergeometric function.

D. POTENTIAL OF A THIN PROLATE ELLIPSOIDAL SHELL

Let us derive analogue of formulas (C6) for prolate systems, e.i. equidensity axisymmetric ellipsoids with axial ratio $Q > 1$. First we shall examine a thin prolate ellipsoidal shell and than summarise the contribution of such shells into the total potential. By the definition the axial ratio of the shell is Q and it has a coordinate m , denoting the shell coordinates R_\star, z_\star as in equation (C4):

$$R_\star^2 + \frac{z_\star^2}{Q^2} = m^2 \quad (\text{D13})$$

Let us define the prolate coordinates as in problem 2.5 of Chapter 2 Binney & Tremaine (2008)

$$R = a \sinh u \sin v, \quad z = a \cosh u \cos v, \quad \phi - \text{azimuthal angle}. \quad (\text{D14})$$

For comparison the oblate coordinates for $Q < 1$ are: $R = a \cosh u \sin v$, $z = a \sinh u \cos v$, ϕ – the same azimuthal angle. For our coordinates we can express $\sin v$ and $\cos v$ from (D14) and use the trigonometrical identical equation:

$$\frac{R^2}{\sinh^2 u} + \frac{z^2}{\cosh^2 u} = a^2. \quad (\text{D15})$$

We are defining our prolate coordinates so, that one of the ellipsoids with $u = \text{const}$ coincide with our thin shell that generates gravitation potential $\delta\Psi$. Let us denote coordinate for this shell as u_* . Than comparing equations (D14) and (D15) for R_* , z_* , u_* we can write for a and u_* :

$$\coth u_* = Q, \quad a = m \csc u_* = m \sqrt{Q^2 - 1}. \quad (\text{D16})$$

All our ellipsoids with $u = \text{const}$ are confocal with the focus $a = m \sqrt{Q^2 - 1}$. We can see that our coordinates are suitable for $Q > 1$, because $\coth u_* > 1$ for all positive u_* . And for oblate coordinates it will be $\tanh u_* = Q < 1$ for all positive u_* .

In order to find the potential $\delta\Psi$ we are to solve the equation $\nabla^2 \delta\Psi = 0$. We shall find the expression for $\nabla^2 \delta\Psi$ in our prolate coordinates. Now we are varying in turn coordinates u, v, ϕ and moving along orthogonal vectors $\hat{\mathbf{e}}_u, \hat{\mathbf{e}}_v, \hat{\mathbf{e}}_\phi$ by the distances $h_u \delta u, h_v \delta v, h_\phi \delta \phi$:

$$h_u = a \sqrt{\cosh^2 u \sin^2 v + \sinh^2 u \cos^2 v}, \quad h_v = a \sqrt{\cosh^2 u \sin^2 v + \sinh^2 u \cos^2 v}, \quad h_\phi = R = a \sinh u \sin v. \quad (\text{D17})$$

After some transformations we have for h_u, h_v :

$$h_u = h_v = a \sqrt{\cosh^2 u - \cos^2 v}. \quad (\text{D18})$$

For comparison we can write down the coefficients for oblate systems in oblate coordinates: $h_u = h_v = a \sqrt{\sinh^2 u + \cos^2 v}$, $h_\phi = a \cosh u \sin v$. Following the equation for gradient:

$$\nabla = \frac{\hat{\mathbf{e}}_i}{h_i} \frac{\partial}{\partial q_i}, \quad q_1 = u, \quad q_2 = v, \quad q_3 = \phi. \quad (\text{D19})$$

we shall write down the gradient of potential $\delta\Psi$:

$$\nabla(\delta\Psi) = \frac{1}{a \sqrt{\cosh^2 u - \cos^2 v}} \left(\frac{\partial(\delta\Psi)}{\partial u} \hat{\mathbf{e}}_u + \frac{\partial(\delta\Psi)}{\partial v} \hat{\mathbf{e}}_v \right) + \frac{1}{a \sinh u \sin v} \frac{\partial(\delta\Psi)}{\partial \phi} \hat{\mathbf{e}}_\phi. \quad (\text{D20})$$

The equation for Laplacian is:

$$\nabla^2 F = \frac{1}{h_1 h_2 h_3} \left(\frac{\partial}{\partial q_1} \left(\frac{h_2 h_3}{h_1} \frac{\partial F}{\partial q_1} \right) + \frac{\partial}{\partial q_2} \left(\frac{h_3 h_1}{h_2} \frac{\partial F}{\partial q_2} \right) + \frac{\partial}{\partial q_3} \left(\frac{h_1 h_2}{h_3} \frac{\partial F}{\partial q_3} \right) \right). \quad (\text{D21})$$

For $h_1 = h_2$ and h_3 all independent of q_3 we can rewrite this equation in the following way:

$$\nabla^2 F = \frac{1}{h_1^2 h_3} \left(\frac{\partial}{\partial q_1} \left(h_3 \frac{\partial F}{\partial q_1} \right) + \frac{\partial}{\partial q_2} \left(h_3 \frac{\partial F}{\partial q_2} \right) \right) + \frac{1}{h_3^2} \frac{\partial^2 F}{\partial^2 q_3}. \quad (\text{D22})$$

Then for the Laplacian of function $\delta\Psi$ we can write down:

$$\nabla^2(\delta\Psi) = \frac{1}{a^2(\sinh^2 u - \cos^2 v)} \left(\frac{1}{\sinh u} \frac{\partial}{\partial u} \left(\sinh u \frac{\partial(\delta\Psi)}{\partial u} \right) + \frac{1}{\sin v} \frac{\partial}{\partial v} \left(\sin v \frac{\partial(\delta\Psi)}{\partial v} \right) \right) + \frac{1}{a^2 \sinh^2 u \sin^2 v} \frac{\partial^2(\delta\Psi)}{\partial^2 \phi}. \quad (\text{D23})$$

We are interested in the potentials, constant over the ϕ and v variables, so we can write down:

$$\begin{cases} \frac{\partial(\delta\Psi)}{\partial v} = 0, \\ \frac{\partial(\delta\Psi)}{\partial \phi} = 0, \\ \nabla^2(\delta\Psi) = 0. \end{cases} \Rightarrow \frac{d}{du} \left(\sinh u \frac{d(\delta\Psi)}{du} \right) = 0 \Leftrightarrow \frac{d(\delta\Psi)}{du} = \frac{A}{\sinh u}, \quad \delta\Psi = A \log \left(\tanh \frac{u}{2} \right) + B. \quad (\text{D24})$$

In order to find constants A and B we are to take the limit of function $\delta\Psi$ at the infinite value of variables R and z , e.i. infinite $r = \sqrt{R^2 + z^2}$. The limit of the potential of our ellipsoidal shell should be:

$$\lim_{r \rightarrow \infty} \delta\Psi = -\frac{G\delta M}{r}, \quad (\text{D25})$$

where δM is the mass of the ellipsoidal shell.

Let us express r in terms of u and v variables:

$$r^2 \equiv R^2 + z^2 = a^2(\sinh^2 u + \cos^2 v), \quad (\text{D26})$$

and find $\sinh u$ from this expression:

$$a^2 \sinh^2 u = r^2 - a^2 \cos^2 v. \quad (\text{D27})$$

Now subtracting (D27) from $a^2 \cosh^2 u$ we can use the hypergeometric identical equation:

$$a^2 \cosh^2 u = r^2 + a^2 \sin^2 v. \quad (\text{D28})$$

Then we shall rewrite $\tanh \frac{u}{2}$ in terms of r and v , using equation (D28):

$$\log\left(\tanh \frac{u}{2}\right) = \frac{1}{2} \log\left(\frac{\sqrt{r^2 + a^2 \sin v} - a}{\sqrt{r^2 + a^2 \sin v} + a}\right). \quad (\text{D29})$$

Now we shall take a Taylor series expansion of $\delta\Psi$ for small $\frac{a}{r}$:

$$\delta\Psi = -A\frac{a}{r} + B + o\left(\frac{a}{r}\right), \quad (\text{D30})$$

To get the limit of $\delta\Psi$ same as in equation (D25) we can write down for constants A and B :

$$A = \frac{G\delta M}{a}, B = 0. \quad (\text{D31})$$

For the points inside our shell the potential is constant and equal to its value on the shell itself. Let us do some hypertrigonometric transformations to get this value:

$$\log\left(\tanh \frac{u_*}{2}\right) = \log\left(Q - \sqrt{Q^2 - 1}\right). \quad (\text{D32})$$

So, the final result for the potential of thin prolate ellipsoidal shell is:

$$\delta\Psi = \begin{cases} \frac{G\delta M}{m\sqrt{Q^2-1}} \log\left(\tanh \frac{u}{2}\right), & u > u_*, \text{ outside;} \\ \frac{G\delta M}{m\sqrt{Q^2-1}} \log\left(Q - \sqrt{Q^2-1}\right), & u \leq u_*, \text{ inside.} \end{cases} \quad (\text{D33})$$

Let us find the mass δM of our shell with the density $\rho(m)$. The semi-axis of the ellipsoid are m and Qm , so the total volume inside the ellipsoid is:

$$V = \frac{4}{3}\pi m^3 Q, \quad (\text{D34})$$

and the volume δV inside the shell is:

$$\delta V = 2\pi Q m \delta(m^2). \quad (\text{D35})$$

Then the mass δM of the shell is:

$$\delta M = 2\pi Q \rho(m) m \delta(m^2). \quad (\text{D36})$$

Now we can rewrite the equation (D33) for the potential of thin prolate ellipsoidal shell using the expression for δM :

$$\delta\Psi = \begin{cases} 2\pi G \rho(m) \frac{Q}{\sqrt{Q^2-1}} \log\left(\tanh \frac{u}{2}\right) \delta(m^2), & u > u_*; \\ 2\pi G \rho(m) \frac{Q}{\sqrt{Q^2-1}} \log\left(Q - \sqrt{Q^2-1}\right) \delta(m^2), & u \leq u_*; \end{cases} \quad (\text{D37})$$

where u_* is the coordinate of the shell and u is the coordinate of the ellipsoid, that is confocal with the thin shell and passes through the point (R_0, z_0) .

D.1. *Gravitational potential for prolate systems*

Now we are ready to summarise the potentials of prolate ellipsoidal shells at the point (R_0, z_0) to get the total potential Ψ . For each shell we have coordinates m, R_*, z_*, u_* of the shell itself, which satisfy the equation (D15), and coordinate of the ellipsoid u_m on which the point R_0, z_0 lies, and this ellipsoid is confocal with the shell. So, the coordinates u_m, R_0, z_0 also satisfy the equation (D15):

$$\frac{R_0^2}{\sinh^2 u_m} + \frac{z_0^2}{\cosh^2 u_m} = m^2 (Q^2 - 1) \quad (\text{D38})$$

Our point (R_0, z_0) lies on the equidensity shell with the coordinate m_0 . Then the point (R_0, z_0) lies outside the shell which coordinate $m < m_0$ and inside the shell which coordinate $m > m_0$. Let us denote as $\delta\Psi_{out}(m)$ the contribution to the total potential Ψ of that shells, for which the point (R_0, z_0) lies outside the shell. Then for such shells our coordinate u_m is grater then the shell coordinate u_* : $u_m > u_*$. The contribution of shells, for which the point (R_0, z_0) lies inside the shell will be denoted as $\delta\Psi_{in}(m)$. Then for this shells our coordinate u_m is less then the shell coordinate u_* : $u_m < u_*$. And the sum of $\delta\Psi_{in}(m)$ is the case $u \leq u_*$ in the formula (D37), and the sum of $\delta\Psi_{out}(m)$ is the case $u > u_*$ in that formula. We shall write down the sum of $\delta\Psi_{in}(m)$ taking into account the definition of function $\mu(m)$ (C5):

$$\sum_{m > m_0} \delta\Psi_{in}(m) = 2\pi G \frac{Q}{\sqrt{Q^2 - 1}} (\mu(\infty) - \mu(m_0)) \log \left(Q - \sqrt{Q^2 - 1} \right). \quad (\text{D39})$$

The sum of $\delta\Psi_{out}(m)$ will be:

$$\sum_{m < m_0} \delta\Psi_{out}(m) = 2\pi G \frac{Q}{\sqrt{Q^2 - 1}} \left(\mu(m) \log \left(\tanh \frac{u_m}{2} \right) \Big|_0^{m_0} - \int_0^{m_0} \mu(m) d \left(\log \left(\tanh \frac{u_m}{2} \right) \right) \right) \quad (\text{D40})$$

Let us rewrite the differential:

$$d \left(\log \left(\tanh \frac{u_m}{2} \right) \right) = \frac{d \cosh u_m}{\sinh^2 u_m} \quad (\text{D41})$$

For $m = m_0$ ellipsoid u_m coincides with the ellipsoid u_* and we can write $\coth u_m = Q$ as in the equation (D16). So we can evaluate the $\cosh u_m = \frac{Q}{\sqrt{Q^2 - 1}}$ for $m = m_0$. And for $m = 0$ to satisfy the equation (D15) we are to set $\coth u_m = \infty$. Summarising equations (D39) and (D40) and taking into account the differential (D41) we can derive the gravitational potential at the point $\Psi(R_0, z_0)$:

$$\Psi(R_0, z_0) = 2\pi G \frac{Q}{\sqrt{Q^2 - 1}} \left(\mu(\infty) \log \left(Q - \sqrt{Q^2 - 1} \right) + \int_{\cosh u_m = \frac{Q}{\sqrt{Q^2 - 1}}}^{\infty} \mu(m) \frac{d \cosh u_m}{\sinh^2 u_m} \right). \quad (\text{D42})$$

Let us rewrite the expressions for $\sinh u_m, \cosh u_m$ in terms of τ, a_0, b_0 :

$$b_0 = Qa_0; \quad \tau + a_0^2 = a_0^2 \sinh^2 u_m (Q^2 - 1) \Rightarrow a_0^2 \cosh^2 u_m (Q^2 - 1) = \tau + b_0^2, \quad d\tau = 2a_0 \sqrt{Q^2 - 1} \sqrt{\tau + b_0^2} d \cosh u_m. \quad (\text{D43})$$

For $m = m_0$ we can write $\sinh u_m = \frac{1}{\sqrt{Q^2 - 1}}$ and than $\tau = 0$. For $m = 0$ and $\cosh u_m = \infty$ we can write $\tau = \infty$. Then the rise of the potential over its central value could be write down as:

$$\Psi(R_0, z_0) - \Psi(0, 0) = \pi G Q a_0 \int_0^{\infty} \mu(m) \frac{d\tau}{(\tau + a_0^2) \sqrt{\tau + b_0^2}}. \quad (\text{D44})$$

We can see that the definitions of a_0, b_0 and the equations (C6) and (D44) for $\Psi(R_0, z_0) - \Psi(0, 0)$ are identical for oblate and prolate systems!

Table 9. Code parameters for NEMO mkkd95 runs.

q	psi0	v0	ra	rck2	rhob	psicut	sigb
q	Ψ_0	v_0	R_a	r_{ck}^2	ρ_b	Ψ_c	σ_b

Table 10. Code parameters for AGAMA Schwarzschild's runs.

DM parameters							
densityNorm	mass	scaleRadius	alpha	beta	gamma	axisRatioY	axisRatioZ
ρ_0	M_{DM}	b_{halo}	γ	η	$-\alpha$	p	Q
Stellar parameters							
W0	mass	scaleRadius	beta	icbeta	ickappa	axisRatioZ	
W_0	M_{stars}	b_p, r_{cA}	β	β_z	κ	q	

E. NOTATIONS FOR PROGRAM CODES PARAMETERS

We can see the vocabulary for program codes parameters in the following tables 9 and 10. The first row of the tables are the codes parameters in bold font and the second row are the Greek letters notations for the parameters used in the paper. Table 9 shows the NEMO mkkd95 code parameters. Table 10 shows the AGAMA Schwarzschild's **modeling** code parameters. The notation for falcON code parameters are the follows:

- **kmax** – k_{max} ,
- **eps** – ϵ .